REVIEW ARTICLE

Open Access

Higher-order mesoscopic self-assembly of fluorinated surfactants on water surfaces

Motomu Tanaka[1,2], Marie Pierre Krafft[3] and Andreea Pasc[4]

Abstract

Surfactants containing fluorocarbon chains have been increasingly studied because they self-assemble into a variety of microscopic and mesoscopic domains and tend to form highly ordered patterns at the air/water interface; these patterns are clearly different from those formed by their hydrocarbon analogs. Focusing on the fluorinated surfactants possessing unique physical characteristics, this review describes the relationship between the line tension and dipole interaction, which is the comprehensive principle governing the pattern formation of two-dimensional self-assemblies. This review further discusses several key experimental and analytical techniques that are useful for characterizing the shape, size, correlation, and viscoelasticity of hierarchical self-assemblies on water surfaces. Finally, several biomedical applications, including biomimetic surface coating, multimodal contrast agents in medical diagnostics, and controlled delivery of gases (O_2 and NO) for oxygenation and antimicrobial effects, are introduced to highlight how the unique physicochemical properties of fluorinated self-assemblies can be applied in materials science.

Higher-order pattern formation by molecular self-assemblies is a universal phenomenon

A wide range of organic molecules (including surfactants, liquid crystals, and diblock copolymers) have various hierarchical two- and three-dimensional patterns and textures[1,2]. For example, circular domains, stripes, and chiral crystal structures have been found in Langmuir monolayers of lipids and surfactants at the air/water interface[3,4]. Three-dimensional lamellae, inversed hexagonal micelles, and bicontinuous cubic phase assemblies of lipids[5,6], liquid crystals[7], and diblock copolymers[8–11] have also been found. Notably, a small set of structural parameters leads to very similar patterns, independent of the detailed molecular structures. For example, Israelachivili, Mitchell, and Ninham theoretically accounted for the shape of self-assembled surfactant aggregates using the following geometric packing constraint: $p = v/Al$, where v is the volume of the hydrophobic core, A is the surface area (area occupied by a head group), and l is the axial length of the surfactant molecule[12]. This simple geometric constraint can be applied to predict the morphology of various supramolecular architectures formed by a wide variety of molecules with different sizes and structures, including phospholipids, liquid crystals, and block copolymers. However, the characteristic length scale and periodicity of patterns can range over several orders of magnitude, from tens of nanometers (e.g., periodicity of phospholipid "ripples")[13] to hundreds of micrometers (e.g., stationary patterns driven by chemical reactions)[14]. As comprehensively summarized by Seul and Andelman from a theoretical viewpoint[2], these patterns are stabilized through interplay between competing intermolecular interactions characterized by the spatial variation of order parameters. As described more explicitly in the following sections, this review specifically focuses on two-dimensional assemblies of fluorinated surfactants on water surfaces because the competition of line tension and dipole interaction plays dominant roles in the formation of various hierarchical structures.

Fluorinated surfactants: What make them unique compared with hydrocarbon analogs?

This review aims to provide a comprehensive overview of the physical principles governing the formation of

Correspondence: Motomu Tanaka (tanaka@uni-heidelberg.de)
[1]Center for Integrative Medicine and Physics, Institute for Advanced Study, Kyoto University, Kyoto, Japan
[2]Physical Chemistry of Biosystems, Institute of Physical Chemistry, Heidelberg University, Heidelberg, Germany
Full list of author information is available at the end of the article

highly ordered patterns by self-assemblies. As an example, we will focus on fluorinated surfactants, which have been shown to form a rich variety of patterns that are distinct from their commonly studied hydrocarbon analogs. Fluorocarbon chains have different structures and physical properties than their hydrocarbon analogs[15–17]. A fluorine atom is bulkier than a hydrogen atom, so ordered fluorocarbon chains have rigid 15/7 helical conformations rather than all-*trans* conformations, as in the case of hydrocarbon chains. The cross-sectional areas of fluorocarbon chains (27–30 Å^2)[218,] are therefore larger than the cross-sectional areas of hydrocarbon chains with all-*trans* conformations (18–21 Å)^2. The cohesion energy between fluorocarbon chains is lower than the cohesion energy between hydrocarbon chains because fluorocarbon chains are less polarizable than hydrocarbon chains. Moreover, the surface potentials of surfactant fluorocarbon chains at the air/water interface are negative with respect to water[19,20], indicating that the molecular dipoles of fluorocarbon chains point in the opposite direction of the molecular dipoles of hydrocarbon chains. Importantly, hydrocarbons and fluorocarbons are both hydrophobic but are totally immiscible; fluorocarbon chains are lipophobic, but hydrocarbon chains are fluorophobic.

The clear differences in physico-chemical properties between fluorocarbons and hydrocarbons and their mutual immiscibility suggest that the self-assemblies of compounds containing fluorocarbon chains should be distinct from those of their hydrocarbon analogs. Kunitake, Ringsdorf, and their coworkers synthesized phospholipids containing fluorocarbon chains and found that these lipids were hardly miscible with lipids containing hydrocarbon chains[21–23]. Riess et al. synthesized various modular single- and double-chain fluorinated surfactants with polar heads derived from phospholipids, amino acids, sugars, polyols and other biomaterials and characterized their physicochemical properties[24,25]. Notably, compounds containing both fluorocarbon and hydrocarbon chains tend to self-assemble into micelles in either fluorocarbon or hydrocarbon solvents[26–28].
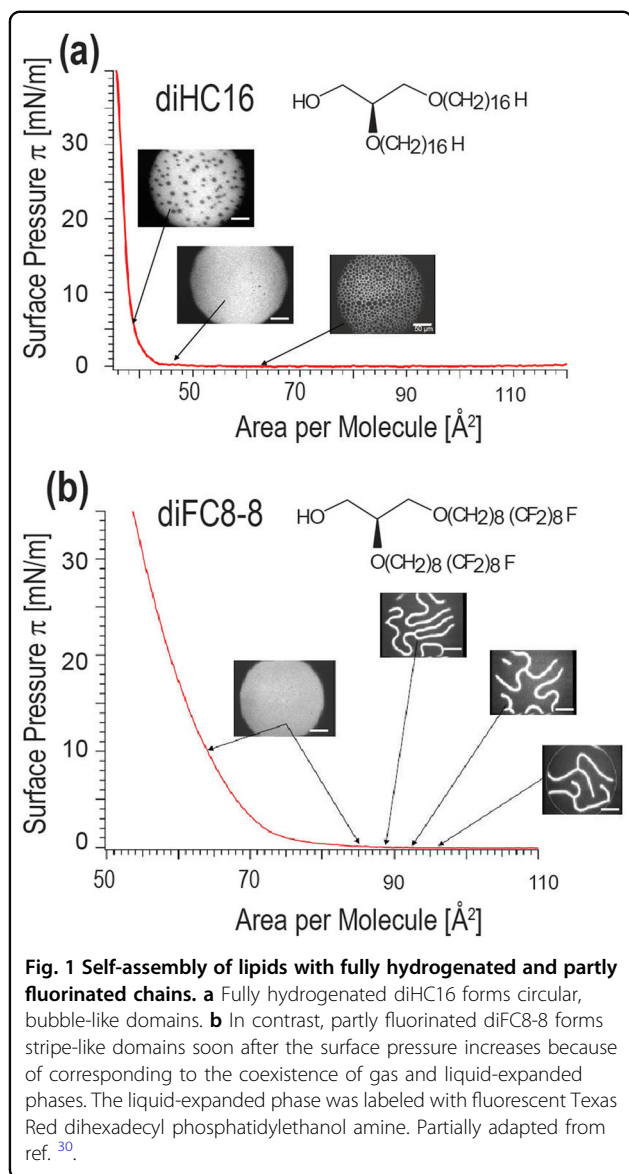
"Microstripes" of fluorinated surfactants in the diluted phase: A dipolar monolayer

How will fluorinated surfactants self-assemble when deposited on a water surface? What are the main differences from the self-assembly of hydrocarbon analogs? To address these questions, Schneider et al. deposited fully hydrogenated dihexadecylglycerol (diHC16) and its half-fluorinated analog (diFC8-8) on a water surface[29]. They observed the self-assemblies of diHC16 and diFC8-8 using a Langmuir film balance coupled to an upright fluorescence microscope and determined the pressure–area isotherms[30].

The pressure–area isotherms of diHC16 and diFC8-8 are shown in Fig. 1a and b, respectively. It can be seen that the area per molecule is higher for diFC8-8 than diHC16 at all surface pressures. At π = 25 mN/m, the areas of one diFC8-8 molecule and one diHC16 molecule are 57 Å^2 and 38 Å^2, respectively, due to the difference between the cross-sectional areas of a fluorocarbon chain (30 Å^2) and a hydrocarbon chain (19 Å^2) and the diFC8-8 and diHC16 molecules each possessing two chains. When the pressure begins to increase, diHC16 has circular "bubble-like" domains at π ≈ 65 Å^2 (Fig. 1a), similar to other lipids with hydrocarbon chains[4]. In contrast, diFC8-8 forms micrometer-thick, "stripe-like" domains at $A ≈ 95$ Å^2 (Fig. 1b). Both types of microdomains are thermodynamically stable and found in the gas–liquid phase coexistence. Further compression of either system causes the film to produce homogeneous fluorescence signals.

Despite the differences in the materials and length scales, the formation of the stripe-like domains of diFC8-8 molecules near the first-order phase transition between the gas and liquid phases follows the same general principle as other condensation transitions[2]. Stretched, stripe-like domains are formed when attractive interactions between molecules become dominant against the mixing entropy. The shapes and thicknesses of stripe-like domains are determined by the competitive interplay between line tension and dipole interactions, as theoretically described by McConnell and Andelman[31,32]. The free energy of line tension F_{line}, represented by the energy contribution by line tension $γ$ to create a phase boundary, is linearly proportional to the peripheral length L of the phase boundary as shown as follows: $F_{line} = γL$. Specifically, the line tension favors circular shapes to minimize the free energy, as found for diHC16 and other hydrocarbon-based surfactants. However, the molecular dipole moment tends to stretch isolated domains because of electrostatic interactions. In this scenario, the contribution of the line tension to the domain energy is as follows: $F_{line/stripe} = \frac{2γ}{D}$, where periodicity D is given as the sum of the thicknesses of the gas (D_G) and liquid (D_L) phases, $D = D_G + D_L$.

Previously, Andelman et al. theoretically predicted that the stripe domains are stabilized through density modulation caused by dipole contributions from the surfactant's head groups[32,33]. However, the dipole contribution from the head groups cannot explain the formation of bubble-like domains by diFC8-8 and microstripes by diHC16 because they have identical –OH head groups. Thus, these data suggest that the dipole moments of the chain termini (–CH$_3$ and –CF$_3$ groups) as well as those of –CH$_2$–CF$_3$– junctions play dominant roles in determining the specific shape and size of domains formed by diFC8-8. The surface potentials of diFC8-8 and diHC16, determined using the Helmholtz equation, $V = \frac{μ}{εA}$[34], have

Fig. 1 Self-assembly of lipids with fully hydrogenated and partly fluorinated chains. a Fully hydrogenated diHC16 forms circular, bubble-like domains. **b** In contrast, partly fluorinated diFC8-8 forms stripe-like domains soon after the surface pressure increases because of corresponding to the coexistence of gas and liquid-expanded phases. The liquid-expanded phase was labeled with fluorescent Texas Red dihexadecyl phosphatidylethanol amine. Partially adapted from ref. [30].

opposite signs, indicating that the dipole moment of diFC8-8 points away from the monolayer toward the air[30], as reported previously[20,35]. In the Helmholtz equation, μ is the effective dipole moment, and A is the area per molecule.

Assuming that the infinitely long stripe domains of the gas and liquid phases with thicknesses D_G and D_L, respectively, are separated by sharp boundaries, the free energy of the stripe geometry can be calculated using Eq. (1):

$$F = \frac{k_B T b^3}{\pi \sqrt{A}} \left[x_L \phi_L^2 + x_G \phi_G^2 \right] - \frac{b^3}{\pi D} (\phi_L - \phi_G)^2 \log \left(\frac{D \sin \pi x}{\pi \sqrt{A}} \right), \quad (1)$$

where x and ϕ are the fraction and surface concentration (mol/m^2) of each phase, $b^3 = \frac{\mu^2 \varepsilon}{k_B T \varepsilon_0 (\varepsilon + \varepsilon_0)}$, and ε and ε_0 are

the dielectric constant near the dipoles and the dielectric constant of water, respectively. The first two terms provide the mean contribution of the electrostatic energy and are therefore independent of D, but the third term is the sum of the intra- and inter-stripe dipolar interactions[36]. The difference between the total free energies of the stripe phase and a reference gas–liquid coexistence is therefore as follows:

$$\Delta F = \frac{k_B T b^3}{\pi D} (\phi_L - \phi_G)^2 \log \left(\frac{D \sin \pi x}{\pi \sqrt{A}} \right) + \frac{2\gamma}{D}. \quad (2)$$

Minimizing ΔF with respect to the periodicity D provides the equilibrium stripe width:

$$D_{eq} = \frac{\pi x \sqrt{A}}{\sin \pi x} \exp \left[\frac{2\pi \gamma}{k_B T b^3 (\phi_L - \phi_G)^2} + 1 \right]. \quad (3)$$

Using the previously reported line tension $\gamma = 1.6 \times 10^{-12}$ N[37] and the experimentally determined surface area and potential values, the equilibrium thickness $D_{eq} \approx 1\,\mu m$ can be calculated using Eq. (3). This equilibrium thickness agrees well with the experimentally determined equilibrium thicknesses ($D_{exp} = 2–8\,\mu m$). Decreasing γ by adding a substitutional impurity such as cholesterol resulted in a significant decrease in D_{exp}, which provides supporting evidence that the competition between dipole interactions and line tension determines the periodicity.

Experimental determination of the shape, size, and long-range order of self-assembled domains

Krafft et al. synthesized various semifluorinated alkanes $C_n F_{2n+1} C_m H_{2m+1}$ (*FnHm* diblocks; Fig. 2a)) based on covalent connections between fluorocarbon (*Fn*) and hydrocarbon (*Hm*) segments[38,39]. These molecules contain no hydrophilic moieties but form stable Langmuir monolayers at the air/water interface[28,40]. It is well established that hydrocarbon-based surfactants tend to form a flat monolayer, which can be treated as a two-dimensional continuum. In contrast, atomic force microscopy (AFM) images of *FnHm* monolayers transferred onto solid substrates indicated that an *FnHm* monolayer consists of monodisperse, disk-like domains with diameters of 20–40 nm[41]. This orientation of molecules was initially debated because both moieties are hydrophobic. Abed et al. claimed that antiparallel stacking of diblocks occurred[42], but X-ray/neutron reflectivity and surface potential measurements indicated that the fluorocarbon chains were in contact with air and the hydrocarbon chains were in contact with water[43–47].

To specifically account for the mesoscopic domain formation, Semenov et al. developed a theoretical model[48] and demonstrated that the micelles are mesoscopic
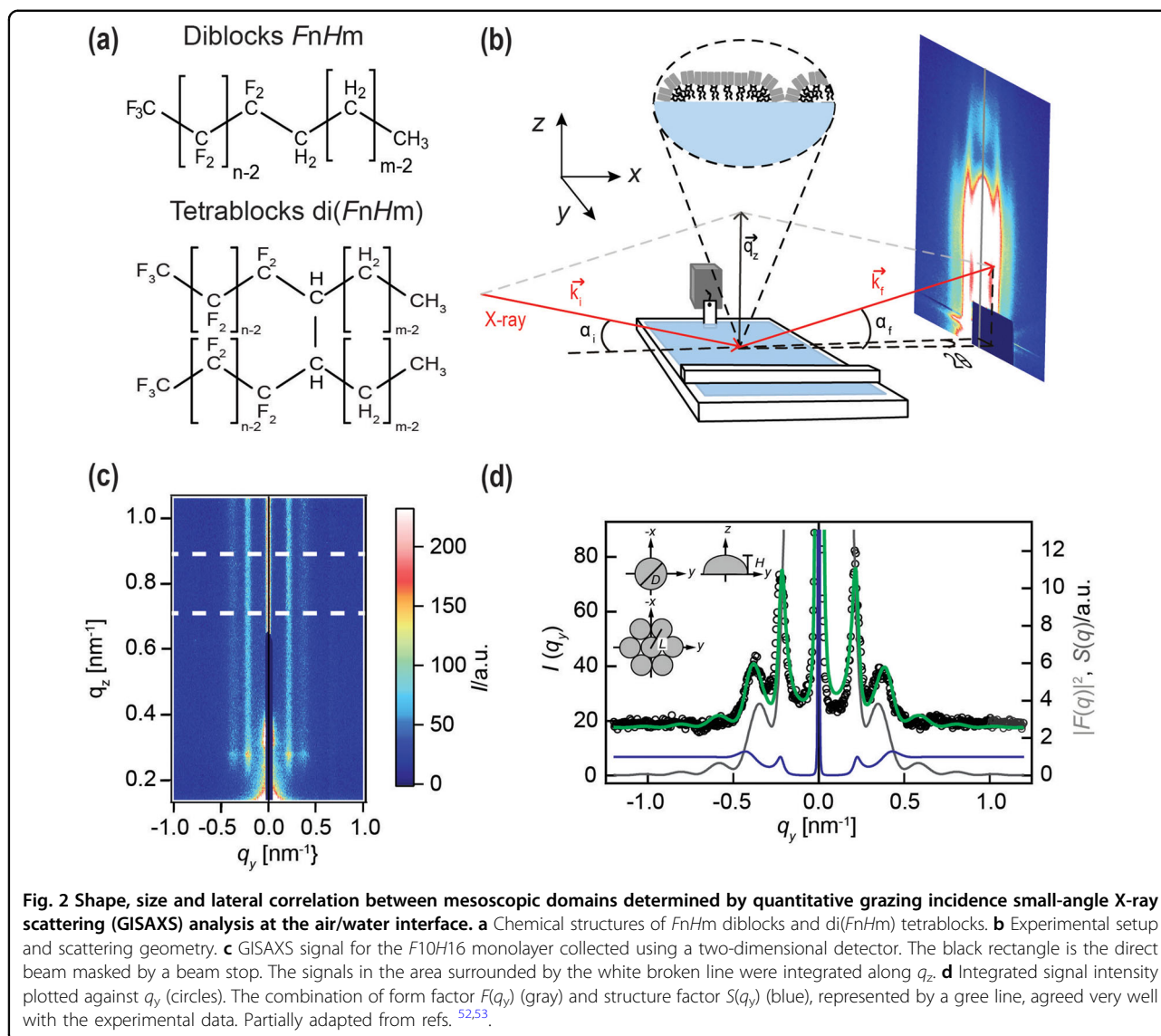
Fig. 2 Shape, size and lateral correlation between mesoscopic domains determined by quantitative grazing incidence small-angle X-ray scattering (GISAXS) analysis at the air/water interface. a Chemical structures of *FnH*m diblocks and di(*FnH*m) tetrablocks. **b** Experimental setup and scattering geometry. **c** GISAXS signal for the *F10H16* monolayer collected using a two-dimensional detector. The black rectangle is the direct beam masked by a beam stop. The signals in the area surrounded by the white broken line were integrated along q_z. **d** Integrated signal intensity plotted against q_y (circles). The combination of form factor $F(q_y)$ (gray) and structure factor $S(q_y)$ (blue), represented by a gree line, agreed very well with the experimental data. Partially adapted from refs. [52,53].

domains of a high density phase of the *FnHm* molecules with vertical orientations (the fluorinated segments being extended toward air and the hydrocarbon segments toward water), the continuous phase is of lower density, and the *FnHm* diblocks are nearly parallel to the water surface. In general, the shape and size of mesoscopic domains are determined by the competitive interplay between line tension and dipole interactions, as described in the previous section. Here, the line tension favors coalescence of circular domains to minimize the tension free energy of line tension, $F_{line} = \gamma L$. However, the repulsive electrostatic interactions between domains contribute to avoiding the coalescence of domains and maintaining their monodispersed size distribution.

Notably, the self-assembled mesoscopic domains of *FnHm* diblocks act as colloidal particles and assemble into hexagonal arrays. Topographic profiles acquired by AFM demonstrate that the mesoscopic domains of *FnHm* diblocks have long-range order beyond their own sizes. However, once a monolayer has been transferred onto a solid substrate, the domains lose translational and rotational degrees of freedoms. Therefore, it is desirable to determine the hierarchical structures of the self-assembled semifluorinated alkanes on a "free" water surface. Among various surface sensitive techniques, grazing incidence small-angle X-ray scattering (GISAXS) is a powerful tool for determining the long-range correlation between self-assembled mesoscopic objects on the water surface that cannot be visualized by optical microscopy[49,50]. Fontaine et al. performed GISAXS measurements of *F8H16* monolayers at the air/water interface. At a surface pressure of π = 5 mN, they identified several

diffraction peaks that were assigned to a hexagonal lattice with a unit length of 33 nm[47]. Bardin et al. found that the lattice parameter increased monotonically as the hydrocarbon chain length increased, suggesting that subtle changes in molecular structure can be used to change the lattice parameter[51]. However, it is noteworthy that the lattice parameter does not directly correspond to the domain size because the discrete domains are separated by the dilute phase. Therefore, quantitative calculations of GISAXS signals are necessary to determine the domain size more accurately.

Figure 2b shows the experimental setup and the scattering geometry for GISAXS measurements at the air/water interface. A monolayer of diblocks *FnHm* or tetrablocks di(*FnHm*) is deposited on the Langmuir film balance and compressed to a surface pressure π. A monochromic synchrotron beam is directed on the interface at incident angle α_i (slightly lower than the critical angle of total reflection), e.g., $\alpha_i = 0.12°$ for 8 keV and $\alpha_i = 0.2°$ for 10 keV, and the scattering signals are detected using a two-dimensional pixel detector. The GISAXS signal for an *F10H16* monolayer is shown in Fig. 2c. The black rectangle near $q_y = 0$ is the direct beam masked by a beam stop. The maximum scattering intensity is $q_z \approx 0.28$ nm^{-1} and called the Yoneda peak. The maximum scattering intensity decreases rapidly as q_z increases. To gain sufficient counting statistics, the signal intensity is integrated between $q_z = 0.7$ and 0.9 nm^{-1} (indicated by white dashed lines), which is sufficiently far from the Yoneda peak and the beam stop. The integrated GISAXS signal is shown in Fig. 2d.

The GISAXS signal intensity $I(q_y)$ can generally be determined from the structure factor $S(q_y)$ and form factor $F(q_y)$ as follows:

$$I(q_y) = A|F(q_y)|^2 \cdot S(q_y). \tag{4}$$

where A is a scaling factor. Form factor $F(q_y)$ reflects the shapes and sizes of the objects, whereas structure factor $S(q_y)$ reflects the lateral organization of the objects. The model used to determine the form factor is selected based on AFM observations. For example, $F(q_y)$ for an oblate hemispheroid with diameter Φ and height H (Fig. 2d inset) is used for the *FnHm* domains[52], with Eq. (5):

$$F(q_x, q_y, q_z\, \Phi, H) = 2\pi \int_0^H \left(\frac{\Phi}{2}\right)^2 \left(1 - \left(\frac{z}{H}\right)^2\right) J_1 \left(\frac{\Phi\sqrt{\left(q_x^2 + q_y^2\right)\left(1 - \left(\frac{z}{H}\right)^2\right)}}{2}\right) exp(-iq_z z)dz. \tag{5}$$

where J_1 is the first-order Bessel function of the first kind. The calculated $F(q_y)$ is shown as a gray line in Fig. 2d.

However, $F(q_y)$ of an oblate hemiellipsoid is used to provide the best fit for di(*FnHm*) tetrablocks[53]. The form factor can be calculated within the framework of the distorted wave Born approximation (DWBA) that considers multiple scattering events caused by the beam, which is larger than the objects[54,55].

The structure factor $S(q_y)$ is modeled in the framework using paracrystal theory. The $S(q_y)$ for *FnHm* is modeled using a two-dimensional hexagonal lattice (the blue line in Fig. 2d)[52], as shown in Eqs. (6) and (7):

$$S(q_x, q_y, L, \sigma) = \frac{(1 - \varphi^2)^2}{\left(1 + \varphi^2 - 2\varphi\cos(q_y L)\right)\left(1 + \varphi^2 - 2\varphi\cos\left(\frac{q_{yL}}{2} + \frac{\sqrt{3}q_{xL}}{2}\right)\right)}, \tag{6}$$

where φ is calculated as follows:

$$\varphi = \exp\left(\frac{-\left(q_x^2 + q_y^2\right)\sigma^2}{2}\right)\exp\left(\frac{-L}{\xi}\right). \tag{7}$$

These equations provide not only the lattice parameter L and its standard deviation σ but also the correlation length ξ, which cannot be determined from the peak positions. For example, the size and correlation length of *F10H16* domains calculated from the fit are $\Phi = 30$ nm and $\xi = 505$ nm, respectively, indicating that the correlation between hemispherical *F10H16* domains can reach a distance that is more than 15 times larger than the domain diameter. As shown by the green line in Fig. 2d, the combination of $F(q_y)$ and $S(q_y)$ shows excellent agreement with the experimental data. Additionally, $S(q_y)$ for di(*FnHm*) was modeled using an orthorhombic (distorted hexagonal) paracrystal lattice[53]. The best model for each system was selected by checking for agreement between the global shape of the GISAXS signals and peak positions using several candidate models. However, the use of the GISAXS technique for mesoscopic self-assembly of small organic molecules is still technically nontrivial for several reasons. The signals can be smeared if the domain size distribution is broad. Moreover, the tradeoff between the signal intensity (counting statistics) and radiation damage should be considered. Nevertheless, GISAXS is an emerging technique that has great potential for identifying the shapes, sizes, and long-range orders of mesoscale self-assemblies of organic molecules that form on water surfaces and cannot be identified otherwise.

Mechanical interactions between self-assembled domains: formation of physical gels

Another remarkable characteristic is that fluorocarbon surfactants and semifluorinated alkanes at the air/water interface have a very poorly compressible monolayer. Maaloum et al. found that the domain structures in films transferred onto solid substrates at $\pi \geq 0.5$ mN/m and

suggested that *FnHm* molecules self-assemble into mesoscopic domains even without compression[41]. In fact, the onset of surface pressure increase is immediately followed by a steep increase with a very small decrease in area. The isothermal compressibility χ of an *FnHm* monolayer at $\pi = 5$ mN/m, $\chi = -\frac{1}{A}\left(\frac{\partial A}{\partial \pi}\right) \approx 10$ m/N, is as low as the isothermal compressibility of a fatty acid in a highly condensed state[56]. Moreover, the domain size Φ and the Φ/L ratio of an *FnHm* determined by GISAXS are remarkably independent of π[52].

These findings suggest that the self-assembled, mesoscopic domains of *FnHm* establish a long-range correlation at a very low π. To quantify the significance of the mechanical interactions between the domains, several research groups have measured the interfacial viscoelasticity of *FnHm* monolayers. Klein et al. used an interface stress rheometer based on a gliding magnetic needle under oscillating magnetic fields[57] and reported that *F12H12* and *F12H20* monolayers are predominantly elastic[58]. Veschgini et al. used another type of interfacial stress rheometer based on a rotating ring coupled to a Langmuir film balance (Fig. 3a)[59]. In this system, an oscillatory shear stress is applied to the monolayer by rotating the ring at frequency ω and driving amplitude γ. The amplitude and phase shift of the ring are used to determine the dynamic surface modulus: $G^*(\omega) = G\prime(\omega) + iG\prime\prime(\omega)$ as a complex function of ω. The real part, the shear storage modulus G', is a measure of the elastic properties, while the imaginary part, the shear loss modulus G'', is a measure of the viscous properties.

The storage (G') and loss (G'') moduli of an *F8H16* monolayer are plotted against the area per molecule A in Fig. 3b. G' and G'' begin to increase at $A \approx 50$ Å^2, but the surface pressure remains at $\pi \approx 0$ mN/m (inset). G' is always larger than G'', indicating that the *F8H16* monolayer is predominantly elastic. This behavior, the formation of two-dimensional gels even in a highly diluted phase, is distinct from the two-dimensional gelation of other surfactant monolayers that occurs only at a high surface pressure for the formation of hydrogen bonds or through cross-linking via entanglement for denatured proteins[59–61]. From the physical viewpoint, the highly unique viscoelastic properties observed in this study can be explained only by the strong repulsions between colloidal particles. In the specific case of *FnHm* and di(*FnHm*) monolayers, the repulsive interactions are dominated by dipole repulsion between CF$_3$ chain termini and CF$_2$–CH$_2$ junctions, preventing the coalescence of surface domains. The systematic variation in the lengths of the *Fn* and *Hm* blocks indicates that the elongation of the *Fn* block from 8 to 12 units increased G' by almost an order of magnitude, but elongating the *Hm* block did not change G' considerably[56]. Genzer et al.[62] found that increasing ordering in the "bulkier" fluorocarbon chain by elongating the chain fr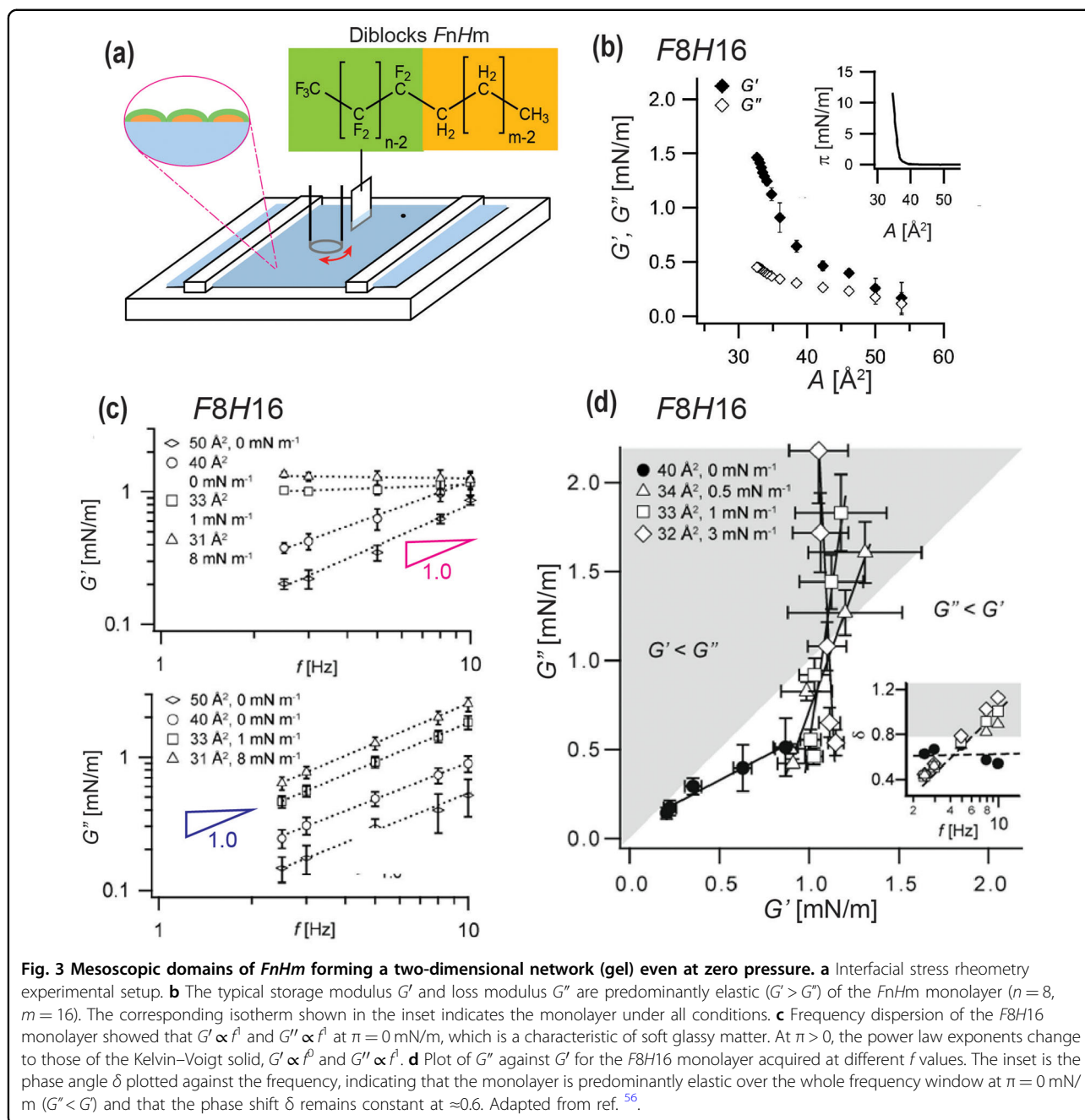om $n = 10$ to 12 did not disturb the lateral packing of hydrocarbon chains. The marked increase in G' caused by elongating the *Fn* block can be attributed to the increase in the domain size due to a higher alignment of the molecular dipoles[30,52]. Fig. 3c shows the frequency dispersion of G' and G'' of *F8H18* monolayers measured under a slight variation in area per molecule: 50 Å^2 ($\pi = 0$ mN/m), 40 Å^2 ($\pi = 0$ mN/m), 33 Å^2 ($\pi = 1$ mN/m), and 31 Å^2 ($\pi = 8$ mN/m). At a surface pressure of zero ($A = 50$ and 40 Å^2), the power law exponents in the double logarithmic plots for both G' and G'' are ≈ 1, which is a characteristic of a soft glassy material[63,64]. Notably, the exponents of G' become zero as soon as the surface pressure becomes positive, but the G'' exponents remain constant at ≈ 1. The observed frequency dispersions at $\pi > 0$, $G' \propto f^0$ and $G'' \propto f^1$ are typical for a classical Kelvin–Voigt solid[65]. When plotting G'' versus G' (Fig. 3d), the film shows a predominant elastic behavior over the whole frequency window at $\pi = 0$ mN/m ($G' < G''$), and the phase shift δ remains at ≈ 0.6 (inset). In contrast, once the film was slightly compressed to $\pi > 0$ mN/m (open symbols), δ shows an increase with increasing frequency f to the region where the film becomes predominantly viscous ($\delta > \pi/2$, $G'' > G'$) beyond a critical frequency. The formation of two-dimensional physical gels through the mesoscopic domains of *FnHm* diblocks, even at $\pi = 0$ mN/m, shares common features with the formation of gels from "hard" particles but has not previously been found for self-assembled films of small organic molecules. These rheological properties can be attributed to strong dipole repulsion between *FnHm* domains.

Higher-order self-assembly in lipid membranes

Sphingolipids, cholesterol, and phospholipids in biological cell membranes form laterally organized functional domains called "rafts."[66] Extensive evidence has shown that mesoscopic/microscopic domains play key roles in complex cellular functions because spatial confinement of functional molecules allows fine-tuning of cooperative polyvalent interactions between biomolecules[67]. Many studies have shown the formation of raft-like domains by the self-assembly of "raft-like" lipid mixtures[68], but most are either polydisperse in size or coalesce into large domains due to line tension. As described above, using lipids containing fluorocarbon chains is a promising strategy to avoid the tension-driven coalescence of domains.

In general, the total free energy F_{total} of a membrane containing domains with diameter D can be described as the sum of the electrostatic energy F_{el} and tension energy F_λ[31] using Eqs. (8)–(10):

$$F_{\text{total}} = F_{\text{el}} + F_\lambda, \tag{8}$$

Fig. 3 Mesoscopic domains of *FnHm* forming a two-dimensional network (gel) even at zero pressure. a Interfacial stress rheometry experimental setup. **b** The typical storage modulus G' and loss modulus G'' are predominantly elastic ($G' > G''$) of the *FnH*m monolayer ($n = 8$, $m = 16$). The corresponding isotherm shown in the inset indicates the monolayer under all conditions. **c** Frequency dispersion of the F8H16 monolayer showed that $G' \propto f^1$ and $G'' \propto f^1$ at $\pi = 0$ mN/m, which is a characteristic of soft glassy matter. At $\pi > 0$, the power law exponents change to those of the Kelvin–Voigt solid, $G' \propto f^0$ and $G'' \propto f^1$. **d** Plot of G'' against G' for the F8H16 monolayer acquired at different f values. The inset is the phase angle δ plotted against the frequency, indicating that the monolayer is predominantly elastic over the whole frequency window at $\pi = 0$ mN/m ($G'' < G'$) and that the phase shift δ remains constant at ≈0.6. Adapted from ref. [56].

where F_{el} is calculated as follows:

$$F_{el} = \pi D(\Delta m)^2 \ln\left(\frac{e^2\delta}{4R}\right), \tag{9}$$
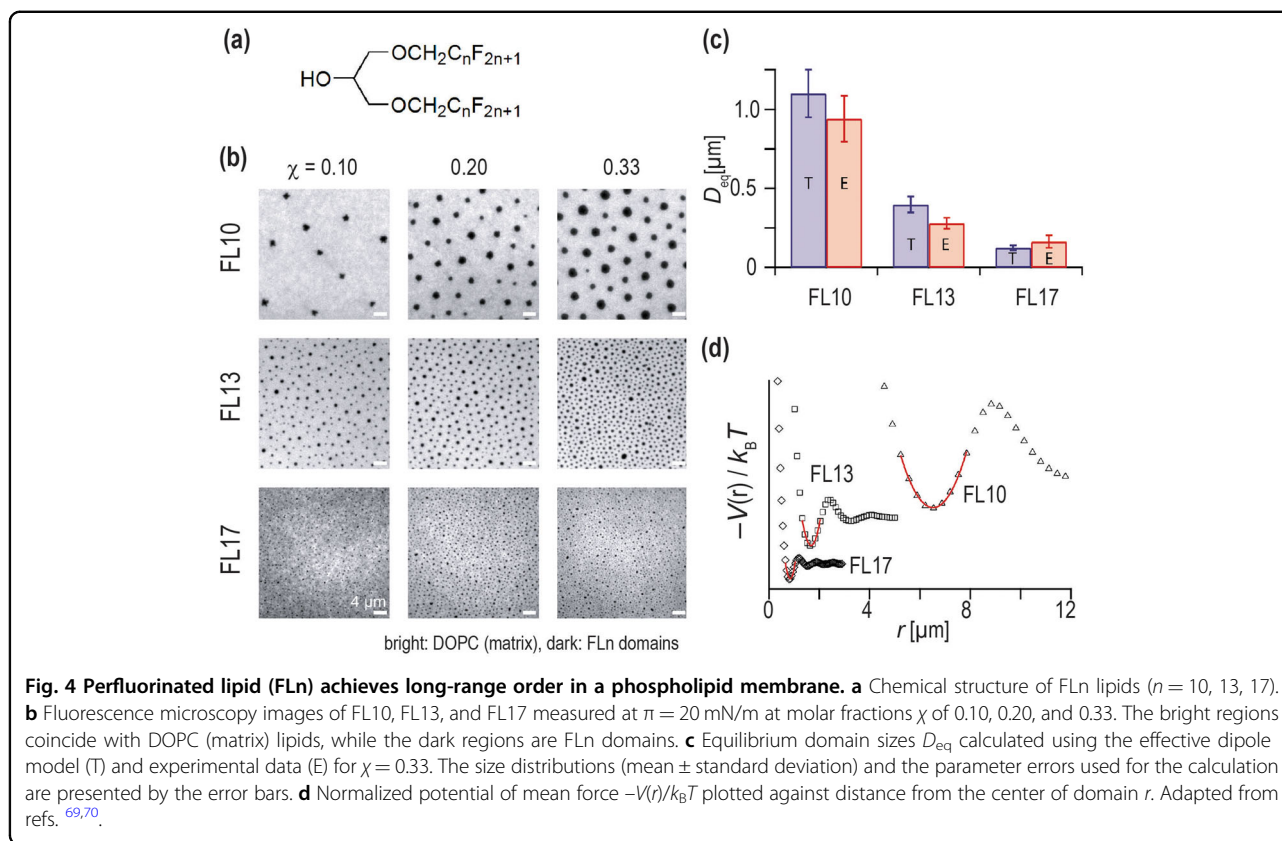
and F_λ is calculated as follows:

$$F_\lambda = \pi D\lambda. \tag{10}$$

where Δm is the difference between the molecular dipole densities of the lipids in the domains and the matrix

lipids, δ is the dipole–dipole distance at the phase boundary, and e is Euler's constant. The line tension λ contains the mismatch between the surface tension $\Delta\gamma$ and the molecular length $\Delta l : \lambda = \Delta\gamma \cdot l + \gamma \cdot \Delta l$. Minimizing the yields therefore provides the equilibrium domain diameter D_{eq} as follows:

$$D_{eq} = \left(\frac{e^3\delta}{4}\right)exp\left(\frac{\lambda}{\Delta m^2}\right). \tag{11}$$

D_{eq} can be calculated because all of the parameters required for the calculation can be determined

Fig. 4 Perfluorinated lipid (FLn) achieves long-range order in a phospholipid membrane. a Chemical structure of FLn lipids ($n = 10, 13, 17$). **b** Fluorescence microscopy images of FL10, FL13, and FL17 measured at $\pi = 20$ mN/m at molar fractions χ of 0.10, 0.20, and 0.33. The bright regions coincide with DOPC (matrix) lipids, while the dark regions are FLn domains. **c** Equilibrium domain sizes D_{eq} calculated using the effective dipole model (T) and experimental data (E) for $\chi = 0.33$. The size distributions (mean ± standard deviation) and the parameter errors used for the calculation are presented by the error bars. **d** Normalized potential of mean force $-V(r)/k_BT$ plotted against distance from the center of domain r. Adapted from refs. [69,70].

experimentally. This suggests that the domain size can be changed by a subtle change in the lengths and densities of the fluorocarbon chains.

To verify the abovementioned hypothesis, Pasc et al. synthesized lipids with perfluorinated anchors (FLn; Fig. 4a) and mixed them with phospholipids with hydrocarbon chains such as dioleoylphosphatidylcholine (DOPC)[69,70]. Fluorescence images of DOPC monolayers incorporating FL10, FL13, and FL17 domains at molar fractions χ of 0.10, 0.20, and 0.33 are shown in Fig. 4b. The domains are round and uniform, showing no sign of coalescence even at a high χ value. The calculated D_{eq} values (T) and experimentally determined domain size D (E) are shown in Fig. 4c. The results agree well; as the fluorocarbon chain is elongated, an increasing n leads to a marked decrease in the domain size[70]. The size of the FL17 domains was close to the optical microscope resolution ($D \approx 0.3$ μm), which was also precisely determined by grazing incidence X-ray diffraction using a Si (111) analyzer crystal[69]. Similar to other colloidal self-assemblies on different length scales[71,72], the long-range correlation between FLn domains can be assessed by calculating the potential of the mean force $V(r)$ within the framework of the inverse work function theorem

using Eq. (12):

$$V(r) \sim -k_BT \ln g(r), \qquad (12)$$

where $g(r)$ is the radial distribution function and calculated as follows:

$$g(r) = \frac{dN(r + dr)}{d(A + dA)} \cdot \frac{N}{A}. \qquad (13)$$

Figure 4d shows $-\frac{V(r)}{k_BT}$ plotted as a function of r for FL10, FL13, and FL17 at $\chi = 0.33$. The position of the first minimum in each curve coincides with the mean center-to-center distance between the nearest neighbors and monotonically decreases as n increases. The potential near the first minimum can be approximated well as a harmonic potential (red line); the significance of inter-domain correlation can be evaluated by the second derivative of the potential, which is only a spring constant for the potential confinement. The spring constant increases by an order of magnitude as the fluorocarbon chain length n increases from 10 to 17, indicating that the smaller FLn domains are confined in steeper potential wells than the

larger FLn domains. Notably, the FL17 domains have distinct minima up to the third order, indicating that the relationships between domains can reach more than an order of magnitude further than the size of a single domain. As expected, the spring constant decreases as χ decreases, and uncorrelated interactions following the Yukawa potential[73] occur at $\chi < 0.05$[70]. More recently, Nakahata et al. demonstrated that tetrablock di($F10H16$) incorporated into a dipalmitoylphosphatidylcholine (DPPC) monolayer affected the lateral organization of DPPC, resulting in large, complex flower-like patterns using fluorescence and Brewster angle microscopy[74].

Higher-order self-assembly for biomimetic coating materials

From the biomaterial science viewpoint, adding functionalities to highly ordered meso-/microdomains of fluorinated lipids embedded in lipid membranes could allow the lipid membranes to act as surrogate surface coatings containing ligand molecules confined in defined, discrete domains. This offers advantages over commonly used surrogate surfaces for studying the adhesive functions of cells. For example, confluent cell monolayers such as monolayers of epithelial cells cannot distinguish between the roles of different ligand−receptor pairs because cells contain complex mixtures of ligand molecules. A surrogate surface based on a supported membrane can allow the surface to be functionalized at precisely controlled interligand densities, but the distribution of functional moieties on the surface is uniform unless a phase-separated membrane is used. However, as described above, the domains of lipid mixtures containing only hydrocarbon chains tend to coalesce due to line tension, resulting in domains with sizes comparable to or even larger than a cell.

Kaindl et al. chemically attached simple mannose to the head group of FL10 (FL10Man; Fig. 5a) and investigated how discrete ligand confinement affected adhesion of the macrophage expressing mannose receptor, which was a 180 kDa C-type lectin containing multiple mannose binding units[75]. Macrophages used multivalent mannose receptor interactions to capture and internalize various mannose-containing proteins[75,76]. A fluorescence image and the potential of mean force for FL10Man at $\chi = 0.33$ are shown in Fig. 5b. FL10Man forms uniform and highly ordered domains similar to FL10 (Fig. 4b), showing no sign of coalescence. This provides clear confirmation that the dipole repulsion between the fluorocarbon chains (not between the head groups) plays a dominant role in preventing coalescence of self-assembled lipid domains. Confocal fluorescence images and microinterferometry images of a murine macrophage adhered to glass substrates coated with three types of lipid membranes are shown in Fig. 5c.

Most of the cells in contact with pure phospholipid (DOPC) membranes could be removed even by a gentle medium exchange. The three-dimensional reconstructed confocal image of a cell shown in the upper left panel of Fig. 5c suggests that the cell is barely deformed and retains its original ellipsoid shape. The micro-interferometry image (lower left of Fig. 5c) indicates that very little cell–substrate contact occurred (the relevant area is indicated with a yellow line for clarity), indicating almost negligible nonspecific cell adhesion to a pure phospholipid membrane. In contrast, when the same macrophages were in contact with the substrate coated with a membrane consisting of only FL10Man ($\chi = 1.0$), the cells were markedly deformed and spread all over the substrate (upper middle part of Fig. 5c). The cell–surface contact area shown as a dark area in the micro-interferometry image (lower middle part of Fig. 5c) is uniform, indicating that the bottom surfaces of the cells adhere uniformly to the membrane-coated substrate. As shown in the upper right image in Fig. 5c, macrophages adhere to and spread on the membrane-displaying domains of FL10Man ($\chi = 0.33$) and extend thin lamellipodia to the surrounding areas. Notably, the adhesion zones visualized by microinterferometry contain uniform dark spots (lower right part of Fig. 5c) with comparable sizes to the FL10Mon domains (Fig. 5b). During the initial spreading process, the spreading front repeatedly sticks and advances rather than continually propagating; this result indicates that the cells find discrete contact points when they are in contact with a new environment. A membrane containing discrete functionalized fluorinated lipid domains could also be used as a coating for a coverless microfluidic channel on which the medium is driven by a surface acoustic wave[77] (not by a pump) to investigate the dynamic adhesion of bacteria onto mannose-functionalized domains (Fig. 5d)[78]. As these meso-/microdomains are formed via self-assembly in the aqueous phase, the domains expressing more complex oligosaccharide moieties can easily be reconstituted in cell-sized, giant lipid vesicles without printing or pre-patterning (Fig. 5f)[29].

Higher-order self-assembly for medical applications

Hierarchically organized self-assemblies of fluorinated molecules have been increasingly studied for medical applications. Various types of supramolecular formulations including gels, vesicles, emulsions, microbubbles, and phase-shift emulsions have been designed as contrast agents for multimodal diagnosis, delivery of energy, delivery of oxygen, nitric oxide and other gases, drugs and biomarkers[16,79,80]. The few recent examples discussed below illustrate the role of such self-assemblies in diagnosis and therapy.
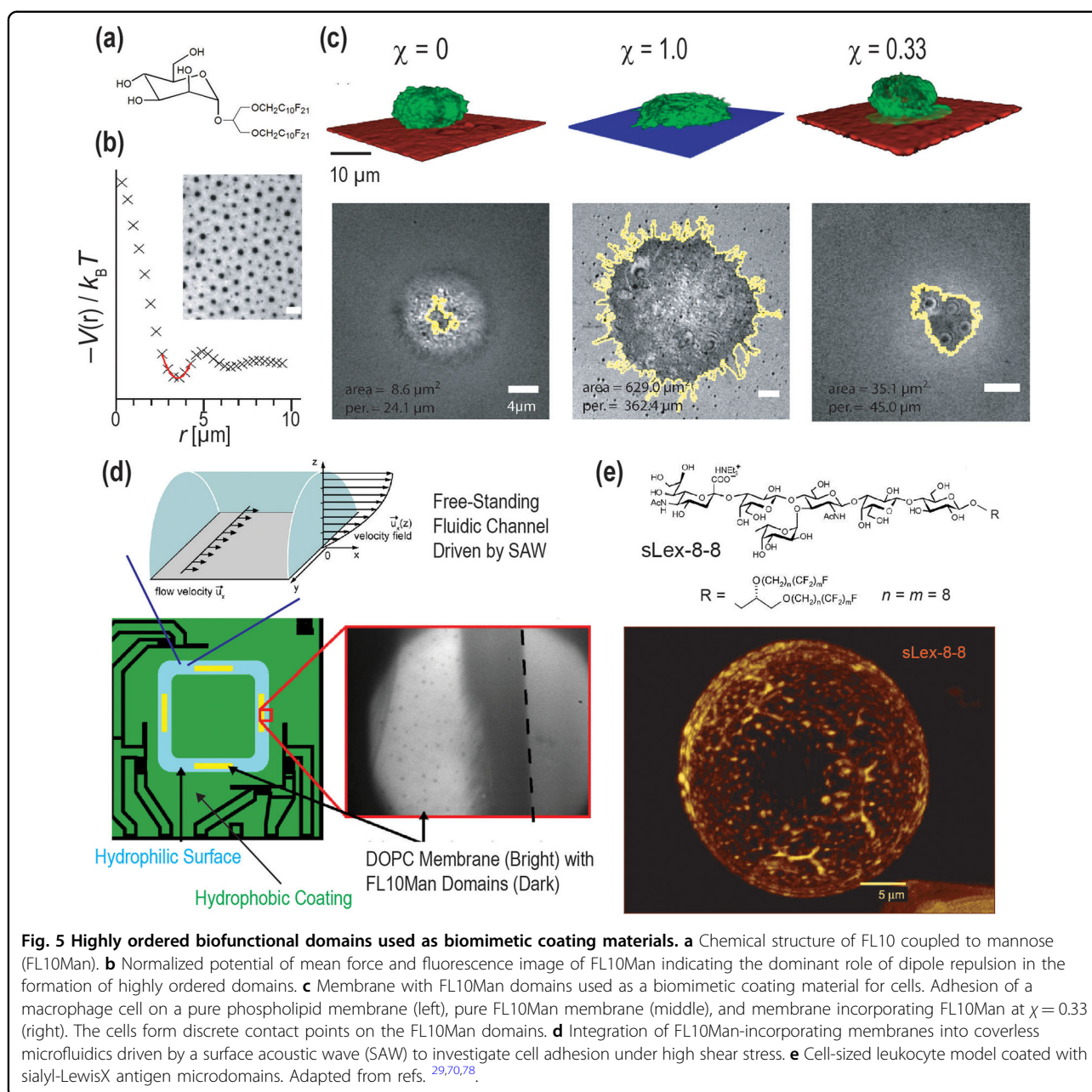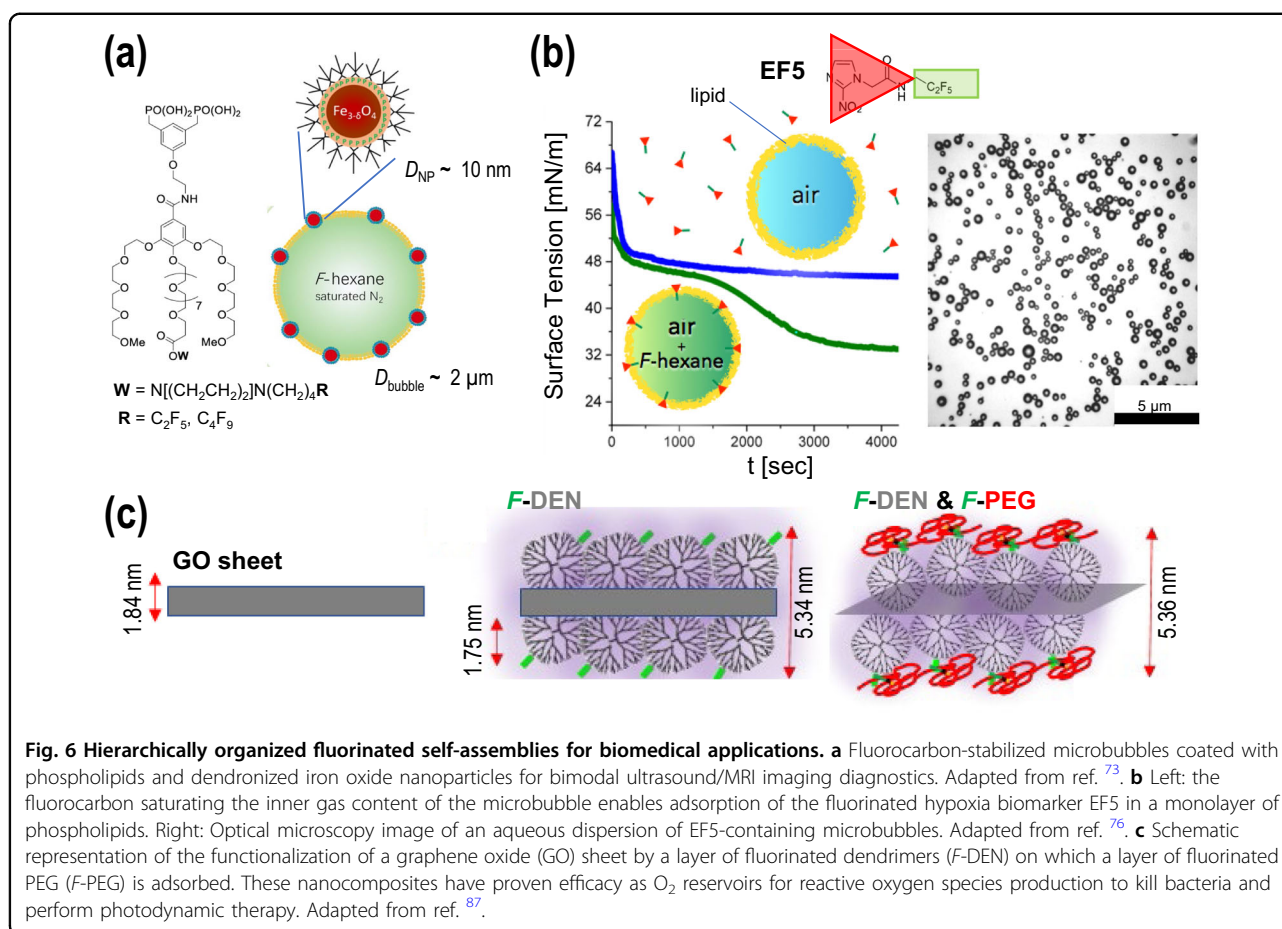
Fig. 5 Highly ordered biofunctional domains used as biomimetic coating materials. a Chemical structure of FL10 coupled to mannose (FL10Man). **b** Normalized potential of mean force and fluorescence image of FL10Man indicating the dominant role of dipole repulsion in the formation of highly ordered domains. **c** Membrane with FL10Man domains used as a biomimetic coating material for cells. Adhesion of a macrophage cell on a pure phospholipid membrane (left), pure FL10Man membrane (middle), and membrane incorporating FL10Man at $\chi = 0.33$ (right). The cells form discrete contact points on the FL10Man domains. **d** Integration of FL10Man-incorporating membranes into coverless microfluidics driven by a surface acoustic wave (SAW) to investigate cell adhesion under high shear stress. **e** Cell-sized leukocyte model coated with sialyl-LewisX antigen microdomains. Adapted from refs. [29,70,78].

Commercial microbubbles currently used for ultrasound diagnostics are coated with shells made of lipids or albumin; however, increasing the control over the microbubble size and stability characteristics remains challenging. Among various lipids, DPPC is chosen because it is in a mechanically stable liquid condensed phase at 37 °C[41]. Microbubbles consisting of phospholipids and self-assembled fluorinated compounds have been applied for medical imaging and therapeutic treatment because the addition of fluorinated compounds increases the lifetime of microbubbles[79]. Pure *FnHm* monolayers tend to collapse under a slight decrease in the surface area due to poor compressibility originating from strong dipole repulsions[56]. Mielke et al. measured the viscoelasticity of mixed monolayers of DPPC and diblock *FnHm* using a dilational rheometer because quantitative measurements of the structure and viscoelasticity of *FnHm* domains in phospholipid microbubbles were technically not possible[81]. The use of a monolayer at the liquid/gas interface can be considered a well-defined mechanical model of microbubbles because the film thickness (≈ 3 nm) is much smaller than the size of microbubbles (~ 1 µm). Although individual *FnHm* domains cannot be visualized by optical microscopy, they accumulate at the boundary of the liquid expanded and liquid condensed phases of DPPC[41]. The

Fig. 6 Hierarchically organized fluorinated self-assemblies for biomedical applications. a Fluorocarbon-stabilized microbubbles coated with phospholipids and dendronized iron oxide nanoparticles for bimodal ultrasound/MRI imaging diagnostics. Adapted from ref. [73]. **b** Left: the fluorocarbon saturating the inner gas content of the microbubble enables adsorption of the fluorinated hypoxia biomarker EF5 in a monolayer of phospholipids. Right: Optical microscopy image of an aqueous dispersion of EF5-containing microbubbles. Adapted from ref. [76]. **c** Schematic representation of the functionalization of a graphene oxide (GO) sheet by a layer of fluorinated dendrimers (*F*-DEN) on which a layer of fluorinated PEG (*F*-PEG) is adsorbed. These nanocomposites have proven efficacy as O_2 reservoirs for reactive oxygen species production to kill bacteria and perform photodynamic therapy. Adapted from ref. [87].

FnHm-DPPC monolayers exhibited viscoelastic properties comparable to those of phospholipid monolayers and persisted under a larger strain under which a pure *F8H16* monolayer collapsed. Therefore, the mixing of *FnHm* with a phospholipid matrix is a promising strategy to improve bubble stability.

More advanced formulations involve the incorporation of iron oxide nanoparticles in phospholipid microbubbles for bimodal ultrasound/MRI contrast agents. This can be achieved by coating nanoparticles with amphiphilic bisphosphonate dendrons bearing three oligo(ethylene glycol) chains terminated with $-C_2F_5$ or $-C_4F_9$ groups (Fig. 6a). The presence of perfluoroalkyl terminal groups is essential to achieve a high stability because the nanoparticles coated with fluorinated dendrons are located inside the interfacial film, while those bearing hydrocarbon dendrons remain on the surface[82].

An increasing number of studies have shown that the presence of a fluorocarbon in the gas phase modulates molecular self-assembly at the gas/liquid interface and significantly enhances the stability of microbubbles. For example, perfluorohexane (*F*-hexane) leads to an increase in the compressibility of pure *FnHm* monolayers by adsorbing to the gas/liquid interface[83]. Moreover, the *F*-hexane-enriched gas phase facilitates the displacement of albumin by DPPC at the gas/water interface under periodic deformations mimicking respiration[84], suggesting that the presence of fluorocarbon gas inside microbubbles is a promising strategy for the formulation of lung surfactant substitutes. As shown in Fig. 6b, the hypoxia biomarker EF5, which is connected to a $-C_2F_5$ group, is readily incorporated from the aqueous phase into DPPC microbubbles with an interior enriched with *F*-hexane[85]. In contrast, EF5 remains in the aqueous phase when the bubble is filled with air. This effective and stable recruitment of EF5–C_2F_5 in the presence of *F*-hexane can be explained by the attractive interactions between the C_2F_5 moiety and *F*-hexane. Notably, the fluorine-functionalized molecules are shown to partly remain trapped in the DPPC monolayer even after the removal of fluorocarbon gas[86].

As shown in Fig. 6c, the self-assembly of oleophobic fluoroalkyl moieties can further be used to design even more complex composite nanomaterials by coating graphene oxide (GO) or oxidized single-walled carbon "nanohorn" with the layers of (i) fluorinated dendrimer (*F*-DEN) and (ii) fluorinated poly(ethylene glycol)

(F-PEG)[87]. The various components/building blocks contribute additively to O_2 adsorption, and the highest O_2-loading capacity is attained by the combination of nanohorns coated with F-DEN and F-PEG. O_2 first adsorbs on the outer F-PEG shell, penetrates into the middle F-DEN region, and eventually reaches the nanohorn core. Irradiation with a light-emitting diode produces singlet oxygen, $^1O_2$, which can be used for oxygen-dependent (e.g., photodynamic) therapy of cancer as well as for fighting bacteria and viruses through $^1O_2$ generation. A similar formulation built from F-DEN, F-PEG and nitrogen-doped carbon nanohorns is devised for efficient nitric oxide delivery utilizing the concentric organization[88].

Summary and perspectives

The general physical principle stabilizing various self-assembled patterns of domains is the interplay between competing intermolecular interactions. At the two-dimensional gas-water interface, self-assembled domains are stabilized by the competition of line tension and dipole interaction. This review focuses on fluorinated surfactants that form unique patterns of self-assembled domains at the air/water interface. These specific patterns, ranging from periodic micrometer-wide stripes to highly correlated mesoscopic hemiellipsoids, are clearly different from those formed by their hydrocarbon analogs. In contrast to the domains of hydrocarbon surfactants, the fluorocarbon domains do not coalesce by compression, indicating that dipole repulsion dominates the line tension in free energy minimization. As demonstrated by the quantitative GISAXS analysis, the shape, size, and lateral correlation between mesoscopic domains are modulated by subtle changes in molecular structures, such as the lengths of fluorocarbon and hydrocarbon chains. Notably, the correlation between mesoscopic domains can reach over a distance that is one order of magnitude larger than the domain diameter. These repulsive, long-range interactions between domains also significantly affect the mechanical properties of fluorinated surfactant layers. Interfacial shear rheology experiments show that the monolayers of semi-fluorinated diblocks form two-dimensional physical gels even at zero surface pressure. This is clearly different from surfactants with hydrocarbon chains that become predominantly elastic only at high surface pressures.

Due to their unique physical principle of self-assembly and pattern formation, fluorinated surfactants can be used in a wide range of biomedical applications. For example, the addition of biofunctional units enables the confinement of ligand molecules in discrete areas, which can readily be transferred to the surface of solid substrates or microfluidic channels. Substrates displaying highly ordered functional mesostructures are ideally suited to study multivalent, cooperative interactions in biological systems, such as cell adhesion caused by multivalent carbohydrate-protein interactions. As discussed in the last section, a wide variety of supramolecular self-assemblies, including gels, vesicles, emulsions, and microbubbles, have been formulated for numerous medical applications, including ultrasound/MRI diagnosis, delivery of medical gases such as O_2 and NO, and the delivery of drugs and biomarkers. The use of self-assembly in the aqueous phase enables the integration of mesoscopic domains not only into flat substrates but also into three-dimensional micelles and cell-sized vesicles, which cannot be achieved by covalent coupling, printing, or patterning techniques.

Author details

[1]Center for Integrative Medicine and Physics, Institute for Advanced Study, Kyoto University, Kyoto, Japan. [2]Physical Chemistry of Biosystems, Institute of Physical Chemistry, Heidelberg University, Heidelberg, Germany. [3]Institut Charles Sadron (CNRS), University of Strasbourg, Strasbourg, France. [4]University of Lorraine (CNRS), L2CM UMR 7053, F-5400 Nancy, France

Author contributions

All authors (M.T., M.P.K., and A.P.) wrote the paper and were involved in all the discussions throughout the preparation of this review article.

Competing interests

The authors declare no competing interests.

Publisher's note

Springer Nature remains neutral with regard to jurisdictional claims in published maps and institutional affiliations.

References

1. Witten, T. A. Structured fluids. *Phys. Today* **43**, 21–28 (1990).

2. Seul, M. & Andelman, D. Domain shapes and patterns: the phenomenology of modulated phases. *Science* **267**, 476–483 (1995).

3. Weis, R. M. & McConnell, H. M. Two-dimensional chiral crystals of phospholipid. *Nature* **310**, 47–49 (1984).

4. Möhwald, H. Chapter 4 - phospholipid monolayers. In *Handbook of biological physics*, (eds Lipowsky, R. & Sackmann, E.) vol. 1., 161–211 (North-Holland, 1995).

5. Luzzati, V., Tardieu, A., Gulik-Krzywicki, T., Rivas, E. & Reiss-Husson, F. Structure of the cubic phases of lipid–water systems. *Nature* **220**, 485–488 (1968).

6. Larsson, K. Cubic lipid-water phases: structures and biomembrane aspects. *J. Phys. Chem.* **93**, 7304–7314 (1989).

7. Kato, T. Self-assembly of phase-segregated liquid crystal structures. *Science* **295**, 2414–2418 (2002).

8. Tanaka, H., Hasegawa, H. & Hashimoto, T. Ordered structure in mixtures of a block copolymer and homopolymers. 1. Solubilization of low molecular weight homopolymers. *Macromolecules* **24**, 240–251 (1991).

9. Bates, F. S. et al. Fluctuations, conformational asymmetry and block copolymer phase behaviour. *Faraday Discuss.* **98**, 7–18 (1994).

10. Alexandridis, P., Olsson, U. & Lindman, B. A record nine different phases (four cubic, two hexagonal, and one lamellar lyotropic liquid crystalline and two micellar solutions) in a ternary isothermal system of an amphiphilic block copolymer and selective solvents (water and oil). *Langmuir* **14**, 2627–2638 (1998).

11. Blanazs, A., Ryan, A. J. & Armes, S. P. Predictive phase diagrams for RAFT aqueous dispersion polymerization: effect of block copolymer composition, molecular weight, and copolymer concentration. *Macromolecules* **45**, 5099–5107 (2012).

12. Israelachvili, J. N., Mitchell, D. J. & Ninham, B. W. Theory of self-assembly of hydrocarbon amphiphiles into micelles and bilayers. *J. Chem. Soc. Faraday Trans. 2 Mol. Chem. Phys.* **72**, 1525–1568 (1976).

13. Zasadzinski, J. A. N., Schneir, J., Gurley, J., Elings, V. & Hansma, P. K. Scanning tunneling microscopy of freeze-fracture replicas of biomembranes. *Science* **239**, 1013–1015 (1988).

14. Ouyang, Q. & Swinney, H. L. Transition from a uniform state to hexagonal and striped Turing patterns. *Nature* **352**, 610–612 (1991).

15. Banks, R. E., Smart, B. E. & Tatlow, J. C. (eds). *Organofluorine Chemistry: Principles and Commercial Applications*. (Plenum Press, New York, 1994).

16. Riess, J. G. et al. Novel fluorocarbon-based injectable oxygen-carrying formulations with long-term room-temperature storage stability. *Adv. Exp. Med Biol.* **345**, 227–234 (1994).

17. Krafft, M. P. & Riess, J. G. Selected physicochemical aspects of poly- and perfluoroalkylated substances relevant to performance, environment and sustainability-Part one. *Chemosphere* **129**, 4–19 (2015).

18. Bunn, C. & Howells, E. Structures of molecules and crystals of fluoro-carbons. *Nature* **174**, 549–551 (1954).

19. Vogel, V. & Möbius, D. Hydrated polar groups in lipid monolayers: effective local dipole moments and dielectric properties. *Thin Solid Films* **159**, 73–81 (1988).

20. Miller, A., Helm, C. A. & Hwald, H. The colloidal nature of phospholipid monolayers. *J. Phys. Fr.* **48**, 693–701 (1987). #xf6.

21. Kunitake, T., Okahata, Y. & Yasunami, S. Formation and enhanced stability of fluoroalkyl bilayer membranes. *J. Am. Chem. Soc.* **104**, 5547–5549 (1982).

22. Higashi, N., Kunitake, T. & Kajiyama, T. Surface-structure and oxygen permeation in mixed multibilayer films of hydrocarbon and fluorocarbon amphiphiles. *Macromolecules* **19**, 1362–1366 (1986).

23. Ringsdorf, H., Schlarb, B. & Venzmer, J. Molecular architecture and function of polymeric oriented systems: models for the study of organization, surface recognition, and dynamics of biomembranes. *Angew. Chem. Int Ed. Engl.* **27**, 113–158 (1988).

24. Riess, J. G. & Krafft, M. P. Fluorocarbons and fluorosurfactants for in vivo oxygen transport (blood substitutes), imaging, and drug delivery. *MRS Bull.* **24**, 42–48 (1999).

25. Riess, J. G. Fluorous micro- and nanophases with a biomedical perspective. *Tetrahedron* **58**, 4113–4131 (2002).

26. Broniatowski, M. & Dynarowicz-Łątka, P. Semifluorinated alkanes — Primitive surfactants of fascinating properties. *Adv. Colloid Interface Sci.* **138**, 63–83 (2008).

27. Krafft, M. P. Large organized surface domains self-assembled from nonpolar amphiphiles. *Acc. Chem. Res.* **45**, 514–524 (2012).

28. Krafft, M. P. & Riess, J. G. Chemistry, physical chemistry, and uses of molecular fluorocarbon— hydrocarbon diblocks, triblocks, and related compounds·

unique "apolar" components for self-assembled colloid and interface engineering. *Chem. Rev.* **109**, 1714–1792 (2009).

29. Gege, C. et al. Functional microdomains of glycolipids with partially fluorinated membrane anchors: Impact on cell adhesion. *ChemPhysChem* **5**, 216–224 (2004).

30. Schneider, M. F., Andelman, D. & Tanaka, M. Stripes of partially fluorinated alkyl chains: dipolar Langmuir monolayers. *J. Chem. Phys.* **122**, 094717 (2005).

31. McConnell, H. M. Structures and transitions in lipid monolayers at the air-water interface. *Annu. Rev. Phys. Chem.* **42**, 171–195 (1991).

32. Andelman, D., Brochard, F. & Joanny, J.-F. Modulated structures and competing interactions in amphiphilic monolayers. *Proc. Natl Acad. Sci.* **84**, 4717–4718 (1987).

33. Andelman, D., Broçhard, F. & Joanny, J. F. Phase transitions in Langmuir monolayers of polar molecules. *J. Chem. Phys.* **86**, 3673–3681 (1987).

34. Brockman, H. Dipole potential of lipid membranes. *Chem. Phys. lipids* **73**, 57–79 (1994).

35. Smondyrev, A. & Berkowitz, M. Molecular dynamics simulation of fluorination effects on a phospholipid bilayer. *J. Chem. Phys.* **111**, 9864–9870 (1999).

36. Keller, D., McConnell, H. & Moy, V. Theory of superstructures in lipid monolayer phase transitions. *J. Phys. Chem.* **90**, 2311–2315 (1986).

37. Benvegnu, D. J. & McConnell, H. M. Line tension between liquid domains in lipid monolayers. *J. Phys. Chem.* **96**, 6820–6824 (1992).

38. de Gracia Lux, C., Gallani, J.-L., Waton, G. & Krafft, M. P. Compression of self-assembled nano-objects - 2D/3D transitions in films of (perfluoroalkyl)alkanes - Persistence of an organized array of surface micelles. *Chem. Eur. J.* **16**, 7186–7198 (2010).

39. de Gracia Lux, C. & Krafft, M. P. Non-polar gemini amphiphiles self-assemble into stacked layers of nano-objects. *Chem. Eur. J.* **16**, 11539–11542 (2010).

40. Gaines, G. L. Surface activity of semifluorinated alkanes: F(CF$_2$)m(CH$_2$)nH. *Langmuir* **7**, 3054–3056 (1991).

41. Maaloum, M., Muller, P. & Krafft, M. P. Monodisperse surface micelles of nonpolar amphiphiles in Langmuir monolayers. *Angew. Chem.* **114**, 4507–4510 (2002).

42. Abed, A. E., Fauré, M. C., Pouzet, E. & Abillon, O. Experimental evidence for an original two-dimensional phase structure: an antiparallel semifluorinated monolayer at the air/water interface. *Phys. Rev. E* **65**, 051603 (2002).

43. Huang, Z. et al. Structural studies of semifluorinated hydrocarbon monolayers at the air/water interface. *J. Chem. Soc. Faraday Trans.* **92**, 545–552 (1996).

44. Broniatowski, M., Miñones, J. Jr & Dynarowicz-Łątka, P. Semifluorinated chains in 2D-(perfluorododecyl)-alkanes at the air/water interface. *J. Colloid Interface Sci.* **279**, 552–558 (2004).

45. Mourran, A. et al. Self-assembly of the perfluoroalkyl-alkane F14H20 in ultrathin films. *Langmuir* **21**, 2308–2316 (2005).

46. de Viguerie, L. et al. Effect of the molecular structure on the hierarchical self-assembly of semifluorinated alkanes at the air/water interface. *Langmuir* **27**, 8776–8786 (2011).

47. Fontaine, P. et al. Direct evidence for highly organized networks of circular surface micelles of surfactant at the air−water interface. *J. Am. Chem. Soc.* **127**, 512–513 (2005).

48. Semenov, A. N., Gonzàlez-Pérez, A., Krafft, M. P. & Legrand, J.-F. Theory of surface micelles of semifluorinated alkanes. *Langmuir* **22**, 8703–8717 (2006).

49. Als-Nielsen J. Refraction and reflection from interfaces. In *Elements of modern X-ray physics*, 69–112, Wiley, Weinheim, Germany (2011)

50. Schultz, D. G. et al. Structure, wrinkling, and reversibility of langmuir monolayers of gold nanoparticles. *J. Phys. Chem. B* **110**, 24522–24529 (2006).

51. Bardin, L. et al. Long-range nanometer-scale organization of semifluorinated alkane monolayers at the air/water interface. *Langmuir* **27**, 13497–13505 (2011).

52. Veschgini, M. et al. Size, shape, and lateral correlation of highly uniform, mesoscopic, self-assembled domains of fluorocarbon–hydrocarbon diblocks at the air/water interface: a GISAXS study. *ChemPhysChem* **18**, 2791–2798 (2017).

53. Abuillan, W. et al. Long-range lateral correlation between self-assembled domains of fluorocarbon-hydrocarbon tetrablocks by quantitative GISAXS. *ChemPhysChem* **20**, 898–904 (2019).

54. Sinha, S. K., Sirota, E. B., Garoff, S. & Stanley, H. B. X-ray and neutron-scattering from rough surfaces. *Phys. Rev. B* **38**, 2297–2311 (1988).

55. Rauscher, M., Salditt, T. & Spohn, H. Small-angle x-ray scattering under grazing incidence: the cross section in the distorted-wave Born approximation. *Phys. Rev. B* **52**, 16855–16863 (1995).

56. Veschgini, M. et al. Existence of two-dimensional physical gels even at zero surface pressure at the air/water interface: rheology of self-assembled domains of small molecules. *Angew. Chem. Int. Ed.* **56**, 12603–12607 (2017).

57. Brooks, C. F., Fuller, G. G., Frank, C. W. & Robertson, C. R. An interfacial stress rheometer to study rheological transitions in monolayers at the air– water interface. *Langmuir* **15**, 2450–2459 (1999).

58. Klein, C. O. et al. Viscoelasticity of semifluorinated alkanes at the air/water interface. *Soft Matter.* **7**, 7737–7746 (2011).

59. Herrmann, M., Schneck, E., Gutsmann, T., Brandenburg, K & Tanaka, M. Bacterial lipopolysaccharides form physically cross-linked, two-dimensional gels in the presence of divalent cations. *Soft Matter.* **11**, 6037–6044 (2015).

60. Schneider, M. F., Lim, K., Fuller, G. G. & Tanaka, M. Rheology of glycocalix model at air/water interface. *Phys. Chem. Chem. Phys.* **4**, 1949–1952 (2002).

61. Vessely, C. R., Carpenter, J. F. & Schwartz, D. K. Calcium-induced changes to the molecular conformation and aggregate structure of β-casein at the air–water interface. *Biomacromolecules* **6**, 3334–3344 (2005).

62. Genzer, J. et al. The orientation of semifluorinated alkanes attached to polymers at the surface of polymer films. *Macromolecules* **33**, 1882–1887 (2000).

63. Sollich, P., Lequeux, F., Hébraud, P. & Cates, M. E. Rheology of soft glassy materials. *Phys. Rev. Lett.* **78**, 2020 (1997).

64. Kröger, M. & Vermant, J. The structure and rheology of complex fluids. *Appl. Rheol.* **10**, 110–111 (2000).

65. Chambon, F. & Winter, H. H. Linear viscoelasticity at the gel point of a crosslinking PDMS with imbalanced stoichiometry. *J. Rheol.* **31**, 683–697 (1987).

66. Simons, K. & Ikonen, E. Functional rafts in cell membranes. *nature* **387**, 569–572 (1997).

67. Mammen, M., Choi, S. K. & Whitesides, G. M. Polyvalent interactions in biological systems: implications for design and use of multivalent ligands and inhibitors. *Angew. Chem. Int. Ed.* **37**, 2754–2794 (1998).

68. Dietrich, C. et al. Lipid rafts reconstituted in model membranes. *Biophys. J.* **80**, 1417–1428 (2001).

69. Oelke, J., Pasc, A., Wixforth, A., Konovalov, O. & Tanaka, M. Highly uniform, strongly correlated fluorinated lipid nanodomains embedded in biological membrane models. *Appl. Phys. Lett.* **93**, 213901 (2008).

70. Kaindl, T. et al. Regulation of adhesion behavior of murine macrophage using supported lipid membranes displaying tunable mannose domains. *J. Phys. Condens. Matter* **22**, 285102 (2010).

71. Quesada-Pérez, M., Moncho-Jordá, A., Martínez-López, F. & Hidalgo-Álvarez, R. Probing interaction forces in colloidal monolayers: Inversion of structural data. *J. Chem. Phys.* **115**, 10897–10902 (2001).

72. Yamamoto, A. et al. A physical biomarker of the quality of cultured corneal endothelial cells and of the long-term prognosis of corneal restoration in patients. *Nat. Biomed. Eng.* **3**, 953–960 (2019).

73. Verwey, E. J. W. Theory of the stability of lyophobic colloids. *J. Phys. Chem.* **51**, 631–636 (1947).

74. Nakahara, H., Krafft, M. P. & Shibata, O. How self-assembled nanodomains can impact the organization of a phospholipid monolayer. Flower-like arrays. *ChemPhysChem* **21**, 1–6 (2020).

75. East, L. & Isacke, C. M. The mannose receptor family. *Biochim. Biophys. Acta* **1572**, 364–386 (2002).

76. Feinberg H., et al. Structural analysis of carbohydrate binding by the macrophage mannose receptor CD206. *J. Biol. Chem.* **296**, 100368 (2021).

77. Wixforth, A. et al. Acoustic manipulation of small droplets. *Anal. Bioanal. Chem.* **379**, 982–991 (2004).

78. Oelke, J. et al. Supported membranes meet flat fluidics: monitoring dynamic cell adhesion on pump-free microfluidics chips functionalized with supported membranes displaying mannose domains. *Materials* **6**, 669–681 (2013).

79. Krafft, M. P. & Riess, J. G. Therapeutic oxygen delivery by perfluorocarbon-based colloids. *Adv. Colloid Interface Sci.* **294**, 102407 (2021).

80. Krafft, M.-P. & Riess, J. G. Stable highly concentrated fluorocarbon gels. *Angew. Chem. Int. Ed. Engl.* **33**, 1100–1101 (1994).

81. Mielke, S. et al. Emergence of strong nonlinear viscoelastic response of semifluorinated alkane monolayers. *Langmuir* **34**, 2489–2496 (2018).

82. Shi, D. et al. Microbubbles decorated with dendronized magnetic nanoparticles for biomedical imaging. Effective stabilization via fluorous interactions. *Beilstein J. Nanotechnol.* **10**, 2103–2115 (2019).

83. Mielke, S. et al. Influence of perfluorohexane-enriched atmosphere on viscoelasticity and structural order of self-assembled semifluorinated alkanes at the air-water interface. *ChemPhysChem* **20**, 1698–1705 (2019).

84. Nguyen, P. N. et al. Counteracting the inhibitory effect of proteins towards lung surfactant substitutes: a fluorocarbon gas helps displace albumin at the air/water interface. *Chem. Commun.* **50**, 11576–11579 (2014).

85. Yang, G., O'Duill, M., Gouverneur, V. & Krafft, M. P. Recruitment and immobilization of a fluorinated biomarker across an interfacial phospholipid film using a fluorocarbon gas. *Angew. Chem. Int Ed.* **54**, 8402–8406 (2015).

86. Liu, X. et al. First quantitative assessment of the adsorption of a fluorocarbon gas on phospholipid monolayers at the air/water interface. *J. Colloid Interface Sci.* **593**, 1–10 (2021).

87. Workie, Y. A. et al. Hierarchical composite nanoarchitectonics with a graphitic core, dendrimer and fluorocarbon domains, and a poly(ethylene glycol) shell as O₂ reservoirs for reactive oxygen species production. *ACS Appl. Mater. Interfaces* **14**, 35027–35039 (2022).

88. Krathumkhet, N., Sabrina, Imae, T. & Krafft, M. P. Nitric oxide gas in carbon nanohorn/fluorinated dendrimer/ fluorinated poly(ethylene glycol)-based hierarchical nanocomposites as therapeutic nanocarriers. *ACS Appl. Bio. Mater.* **4**, 2591–2600 (2021).